

Spatiotemporal imaging of anisotropic charge transfer in photocatalyst particles

Can Li (✉ canli@dicp.ac.cn)

State Key Laboratory of Catalysis, Dalian National Laboratory for Clean Energy, Dalian Institute of Chemical Physics, Chinese Academy of Sciences <https://orcid.org/0000-0002-9301-7850>

Ruotian Chen

Dalian Institute of Chemical Physics, Chinese Academy of Sciences

Zefeng Ren

State Key Laboratory of Molecular Reaction Dynamics, Dalian Institute of Chemical Physics, Chinese Academy of Sciences

Yu Liang

State Key Laboratory of Molecular Reaction Dynamics, Dalian Institute of Chemical Physics, Chinese Academy of Sciences

Thomas Dittrich

Helmholtz-Zentrum-Berlin for Materials and Energy

Shan Pang

State Key Laboratory of Catalysis, Dalian National Laboratory for Clean Energy, Dalian Institute of Chemical Physics, Chinese Academy of Sciences

Yue Zhao

State Key Laboratory of Catalysis, Dalian National Laboratory for Clean Energy, Dalian Institute of Chemical Physics, Chinese Academy of Sciences

Hongyu An

Dalian Institute of Chemical Physics

Guanhua Zhang

State Key Laboratory of Molecular Reaction Dynamics, Dalian Institute of Chemical Physics, Chinese Academy of Sciences

Fengtao Fan

Dalian Institute of Chemical Physics

Physical Sciences - Article

Keywords: photocatalysts, solar fuel production, photocatalyst particles

Posted Date: April 13th, 2021

DOI: <https://doi.org/10.21203/rs.3.rs-251007/v1>

License:  This work is licensed under a Creative Commons Attribution 4.0 International License.

[Read Full License](#)

Version of Record: A version of this preprint was published at Nature on October 12th, 2022. See the published version at <https://doi.org/10.1038/s41586-022-05183-1>.

Abstract

Water-splitting reactions using photocatalyst particles are promising routes for solar fuel production¹⁻⁴. Photoinduced charge transfer from a photocatalyst to catalytic surface sites is key in ensuring photocatalytic efficiency⁵; however, it is challenging to understand this process, which spans a wide spatiotemporal range from nanometers to micrometers and from femtoseconds to seconds⁶⁻⁸. Although the steady-state charge distribution on single photocatalyst particles has been mapped using microscopic techniques⁹⁻¹¹ and the averaged charge transfer dynamics in photocatalyst aggregations have been revealed via time-resolved spectroscopy^{12,13}, spatiotemporally evolving charge transfer processes in single photocatalyst particles cannot be tracked, and the mechanism of charge transfer is unknown. Here, we report spatiotemporally resolved surface photovoltage measurements on Cu₂O photocatalyst particles to map complete charge transfer processes throughout the femtosecond to second time scale at the single-particle level. We found that photogenerated electrons are transferred to the catalytic surface ballistically on a sub-picosecond timescale and are retained at this location for the duration, whereas photogenerated holes are transferred to a spatially separated surface and stabilized via selective trapping on a microsecond timescale. We demonstrate that these ballistic electron transfer and anisotropic trapping regimes, which challenge the classical perception of the drift–diffusion model, contribute to efficient charge separation in photocatalysis and improve the photocatalytic performance. We anticipate our findings to demonstrate the universality of other photoelectronic devices and facilitate the rational design of photocatalysts.

Main Text

Imaging structure-related charge transfer

We first sought to optimize charge separation behavior of representative Cu₂O photocatalyst particles¹⁴ via facet engineering and defect control (Fig. 1a). Facet engineering offers potential for anisotropic charge transfer^{4,15} and enables possible spatial control of defects owing to facet-dependent defect formation¹⁶.

We performed facet engineering by tuning the ratio between the {001} and {111} facets of the Cu₂O particles; consequently, the morphology of the Cu₂O particles evolved from cube to octahedron (Extended Data Figs. 1a–c). To scrutinize the morphological effect on surface charge distribution, we mapped the surface photovoltage (SPV)¹⁷ signals under continuous illumination by surface photovoltage microscopy (SPVM) of either positive SPV-denoted photogenerated holes or negative SPV-denoted photogenerated electrons¹⁰. Fig. 1b shows that more photogenerated electrons are accumulated on the {001} facet of the Cu₂O cube than on the {111} facet of the octahedron. This result can be ascribed to the larger surface built-in electric field in the p-type depletion layer of the {001} facet owing to the higher copper vacancy (V_{Cu}) concentration¹⁸, based on the comparison of Kelvin probe force microscopy (KPFM) images (Extended Data Fig. 1d) and density functional theory (DFT) calculations (Extended Data Fig. 2). More

importantly, the facet-dependent V_{Cu} formation generates interfacet built-in electric fields in Cu_2O particles bounded with $\{001\}$ and $\{111\}$ facets, as evidenced by the surface potential difference between the two facets (Extended Data Fig. 1d). Interestingly, the built-in electric fields vary with the facet ratios and become prominent in the configuration as the $\{111\}/\{001\}$ ratio increases (Extended Data Fig. 1f). Consistent with this, anisotropic charge transfer is observed on polyhedral particles and optimized in the truncated octahedral configuration (Fig. 1c and Extended Data Figs. 1e,g). The good correlation between the interfacet potential difference and the anisotropic SPV signals shows that the interfacet built-in electric fields contributed to the anisotropic charge transfer (Extended Data Fig. 1h).

However, only electrons can be observed on the surface after facet engineering. Hence, we introduced a strategy for spatially controllable defect engineering to selectively extract holes onto the surface. We incorporated hydrogen into Cu_2O to compensate for V_{Cu} and form hydrogenated copper vacancy ($\text{H}-V_{\text{Cu}}$) defects¹⁹ using an electrochemical method (Extended Data Fig. 3a) while maintaining the same particle morphology and size (Extended Data Fig. 3b). X-ray photoelectron spectroscopy (XPS) and Auger Cu LMM spectra verified the compensation of V_{Cu} defects by ($\text{H}-V_{\text{Cu}}$) defects, consistent with the observation that the proportions of Cu^0 and Cu^{2+} increased and decreased, respectively (Extended Data Figs. 3c-e).

We discovered that moderate ($\text{H}-V_{\text{Cu}}$) incorporation resulted in efficient spatial separation of photogenerated electrons and holes on the $\{001\}$ and $\{111\}$ facets, respectively (Fig. 1d and Extended Data Fig. 4a). Nonetheless, extreme ($\text{H}-V_{\text{Cu}}$) incorporation resulted in the disappearance of surface electrons and the spreading of holes over the entire surface of the particle (Fig. 1e). We denote the three types of defect-engineered particles in Figs. 1c-e as $\text{E}-\text{Cu}_2\text{O}$, $\text{EH}-\text{Cu}_2\text{O}$, and $\text{H}-\text{Cu}_2\text{O}$ based on their surface charge distribution. Fig. 1f shows the SPV signal distributions across the $\{111\}$ and $\{001\}$ facets of the three particles. As the ($\text{H}-V_{\text{Cu}}$) incorporation increased, the SPV signals of -10 mV on the $\{111\}$ facet underwent immediate sign reversal and enhanced to 40 mV, followed by a slow enhancement to 50 mV. By contrast, the SPV signals of -40 mV on the $\{001\}$ facet initially decreased slightly to -35 mV but increased to 25 mV with further ($\text{H}-V_{\text{Cu}}$) incorporation. The facet-dependent SPV variations suggest spatially prior ($\text{H}-V_{\text{Cu}}$) incorporation into the $\{111\}$ facets, as predicted by DFT calculations (Extended Data Fig. 2).

To identify the non-uniform defect distributions, we probed the V_{Cu} -related Raman intensity associated with the V_{Cu} density by confocal Raman microscopy (Extended Data Figs. 4b-f)²⁰. Fig. 1g shows a quantitative comparison of the SPV signals and V_{Cu} density, whose decrease corresponds to the formation of ($\text{H}-V_{\text{Cu}}$). Clearly, ($\text{H}-V_{\text{Cu}}$) defects were selectively incorporated into the $\{111\}$ facets of $\text{EH}-\text{Cu}_2\text{O}$ as well as into both the $\{111\}$ and $\{001\}$ facets of $\text{H}-\text{Cu}_2\text{O}$, consistent with the variations in the SPV signals. The defect distributions of the $\text{EH}-\text{Cu}_2\text{O}$ particle shown in Fig. 1h yielded a strong spatial correlation with the SPV distributions shown in Fig. 1d, indicating that the anisotropic defects contributed to the efficient spatial separation of electrons and holes on the photocatalyst surface.

To confirm the efficient charge separation in EH-Cu₂O, we measured the localized charge separation with modulated light on particles having {001} and {111} facets parallel to the substrate (Extended Data Fig. 5a) so that the possible effect of the tip-sample geometry and the diffusion process (almost parallel to the light direction)¹⁰ can be eliminated. The modulated SPV signals agreed well with the steady-state SPV results in terms of both magnitude and sign (Extended Data Fig. 5b), confirming efficient charge separation. Furthermore, we measured the facet-dependent photogenerated charge transport using photoconductive atomic force microscopy²¹ and demonstrated that the photogenerated holes and electrons can be selectively extracted to the {111} and {001} facets, respectively (Extended Data Fig. 5c). In addition, the dependence of SPV signals on light power was significantly different for the two facets (Extended Data Fig. 5d), suggesting different mechanisms for electron and hole transfer.

Imaging of ultrafast electron transfer

We investigated the spatiotemporal origin of the efficient charge separation in EH-Cu₂O. To access the ultrafast charge transfer dynamics in the femtosecond–nanosecond time window, we used time-resolved photoemission electron microscopy (TR-PEEM)^{22,23}, which has not yet been applied to photocatalyst particles. We used 2.4 eV pulses for photoexcitation and 4.8 eV pulses to probe excited electrons, whose energy was insufficient for the emission of electrons from the valence band and V_{Cu} states (Extended Data Figs. 6a,b). Fig. 2a shows a series of photoemission electron images of a single EH-Cu₂O particle captured at different pump-probe delays. Such images provide snapshots for creating movies (Supplementary Movie) and clearly show the anisotropic electron transfer dynamics on the particle, where the photoelectron density is higher on the {001} facet than on the {111} facet.

We plotted the photoelectron intensity vs. time delay measured on the {001} and {111} facets of the EH-Cu₂O particles (Fig. 2b and Extended Data Figs. 6c,d). Similar photoelectron signals were obtained from the lateral and top {111} facets (Extended Data Fig. 6d), indicating that the effect of the distorted electric field in PEEM imaging was negligible. Immediately after the pump pulse excitation, the surface electrons increased at the {001} facet but decreased on the {111} facet within ~0.5 ps. This is indicative of ultrafast electron transfer from the {111} to {001} facets. Electron transfer is expected owing to the formation of a built-in electric field from the {001} to {111} facets with a strength of up to 1.7 kV/cm (Extended Data Figs. 7a–c). However, ultrafast transport is not expected from the conventional drift–diffusion model, even though it has long been regarded as the dominant charge separation mechanism in photocatalysis¹¹. Simulation results showed that the drifts of equilibrium and non-equilibrium carriers in the interfacet built-in electric field were on the time scales of ~150 and ~10 ps, respectively (Extended Data Fig. 7d), which were significantly longer than those observed experimentally. Therefore, we ascribed the ultrafast charge transfer to the ballistic transport regime, in which the carriers propagated at extremely high speeds^{24,25}. The speed of interfacet charge transfer was on the order of 10⁶ m/s, consistent with ballistic transport in p–n junctions²⁴. Furthermore, we observed some non-thermalized hot electrons on the {001} facets within 0.5 ps (Extended Data Fig. 6e), which further supported the occurrence of ballistic transport²⁵. In the subsequent 100 ps, we observed gradually increasing electron

signals on both facets. The time scale was consistent with the drift process of thermalized carriers (Extended Data Fig. 7d), and therefore the increase of electrons on the surface results from the drift of electrons from bulk to surface in p-type space charge region of each facet. Subsequently, the signals decayed on both facets owing to charge recombination or electron trapping at low-energy surface states, where photoelectrons were undetectable²⁶.

Fig. 2c shows spatially resolved and ultrafast SPV dynamics extracted from the peak shifts at different delay times via photoelectron spectroscopy (Extended Data Figs. 6f,g)²⁷. The ballistic electron transfer from the {111} to {001} facets generated an SPV exceeding 100 mV, surpassing the maximum photovoltage limit (~50 mV) in the drift model that was established by the potential difference between the two facets (Extended Data Fig. 7). The anomalously large SPV demonstrated that the ballistic regime was significantly more effective than the drift for charge separation. In the following 10 ps, the rapid changes toward the positive SPV on both facets could be interpreted as fast carrier diffusion²⁸ originating from the Demer effect¹⁰. Subsequently, the negative SPV signals on the {001} facet remained almost unchanged at ~100 ps, followed by a slow decay on the 1 ns timescale. Combining the evolution of the SPV and the photoelectron signals in this time window enabled most electrons on the {001} facets from the ballistic regime to be stabilized for a long lifetime owing to the subsequent drift and trapping processes. Hence, -50 ± 15 mV SPV signals were observed in the equilibrium state. As such, the SPV signals on the {111} facets changed from positive to negative on a timescale of ~200 ps and subsequently stabilized to -10 ± 20 mV.

Visualization of anisotropic trapping

Comparing the SPV signals of EH-Cu₂O at 1 ns (Fig. 2c) and hundreds of milliseconds (Extended Data Fig. 5b), we found good agreement on the {001} facet but disagreement on the {111} facet. The comparison shows that the steady-state electrons on the {001} facet originated from ballistic electron transfer. The disagreement from the {111} facet implies that the SPV signals changed from -10 to 40 mV in the nanosecond–millisecond time window, where defect-induced charge separation typically occurs²⁹.

To directly observe the charge transfer process on nanosecond to millisecond time scales, we performed transient SPV spectroscopy analysis of EH-Cu₂O (Fig. 3a)³⁰. At excitations above the bandgap (~2.04 eV, as determined from the Tauc plots shown in Extended Data Fig. 8d), the SPV signals were negative over a nanosecond timeframe and then reversed to positive as time progressed to the order of microseconds (e.g., ~2 μs at 2.8 eV in Fig. 3b). The reversed SPV signals, rationalizing SPV variations on the {111} facet, were assumed to be associated with $(H-V_{Cu})$ -induced trapping localized on the {111} facet.

We determined the anisotropic trapping processes on the {001} and {111} facets of EH-Cu₂O particles based on sub-bandgap excitations, which typically induce defect-related SPV signals¹⁷. The difference in the absorption edges of the two facets (Extended Data Figs. 8a-f) enabled us to resolve facet-dependent trapping; negative SPV transients at photon energies below 1.9 eV and positive SPV transients at photon

energies near 2.0 eV, as shown in Fig. 3a, occurred owing to selective trapping on the {001} and {111} facets, respectively. For the {001} facets, the negative SPV signals throughout the time scales from nanosecond to millisecond (red line in Fig. 3b) can be assigned to hole trapping by V_{Cu} defects and the drift of electrons in p-type SCR (Extended Data Fig. 8g). By contrast, positive SPV signals on {111} facets (blue line in Fig. 3b) provide evidence regarding the trapping of photogenerated electrons by $(H-V_{Cu})$ defects from the surface states (Extended Data Fig. 8g). The $(H-V_{Cu})$ defects were assumed to be primarily distributed within 60-nm depth beneath the {111} surface (Extended Data Fig. 8d), thereby initiating localized hole transfer to the {111} surface²⁹. The timescales for hole trapping by V_{Cu} and electron trapping by $(H-V_{Cu})$ were a few nanoseconds and tens of microseconds, respectively, in accordance with the observed inversion of SPV signals at super-bandgap excitation (as shown by green line in Fig. 3b). Therefore, we concluded that the steady-state holes on the {111} facets originated from the $(H-V_{Cu})$ -induced charge separation process.

The data above allowed us to completely present the complex charge transfer processes in an EH-Cu₂O photocatalyst (Extended Data Fig. 8h), including ballistic electron transfer to the {001} facets (< 0.5 ps), fast carrier diffusion (~10 ps), charge separation in SCR (~100 ps), selective hole trapping by V_{Cu} on the {001} facets (ns), and selective electron trapping by $(H-V_{Cu})$ on the {111} facets (μ s). Therefore, we can determine that the efficient spatial separation of photogenerated electrons and holes on the {001} and {111} facets was due to the spatiotemporally anisotropic charge transfer mechanism, i.e., ultrafast ballistic electron transfer to the {001} facets and slow defect-induced hole transfer to the {111} facets.

Selective co-catalyst loading and photocatalytic performance

The spatially separated electrons and holes in EH-Cu₂O enabled selective co-catalyst loading¹⁵. Hence, we selectively deposited Au co-catalysts on the {001} facets of EH-Cu₂O particles via photoreductive reactions (Fig. 4a and Extended Data Fig. 9a). The SPVM image in Fig. 4b shows that both electron transfer to the {001} facets and hole transfer to the {111} facets are enhanced after asymmetric Au deposition, and the enhancements were statistically quantified to be 25 mV (-35 to -60 mV) on the {001} facet and 20 mV (40 to 60 mV) on the {111} facet (Fig. 4c). We attributed the increased SPV signals to the amplified built-in electric field by selective Au deposition, based on the observation of increased surface potential at the Au deposition site (Extended Data Figs. 9d-f). By comparison, Au deposition on the E-Cu₂O and H-Cu₂O particles indicated less selectivity and did not lead to improved charge separation (Extended Data Fig. 9). Thus, anisotropic defect engineering can be applied for rational co-catalyst assembly, which would further improve charge separation.

Finally, we investigated the effect of anisotropic charge transfer on the photocatalytic performance. We quantitatively described the driving force of anisotropic charge transfer using the vector sum of spatially resolved SPV signals³¹ and monitored photocatalytic hydrogen generation using engineered Cu₂O particles (Extended Data Fig. 10). Fig. 4d shows that the anisotropic charge transfer governs the photocatalytic performance. Two major steps improved the activity significantly: anisotropic facet and

defect engineering, which simultaneously ensured efficient ballistic electron transfer and defect-induced hole transfer to spatially separated surfaces. Moreover, these strategies enabled rational co-catalyst assembly, which further improved the photocatalytic performance.

Conclusions

By visualizing anisotropic charge transfer throughout the femtosecond to second time scale, we demonstrated that ballistic electron transfer and spatially selective trapping were the dominant mechanisms for efficient charge separation in photocatalysis, and that they can be controlled through rational engineering of anisotropic facets and defects. The ability to spatiotemporally track charge transfer enables a new experimental method for understanding the complex mechanisms in energy conversion devices. The widely accepted drift–diffusion model is not expected to show the ballistic and selective trapping regimes observed; however, these regimes are effective and may be universal for other photocatalytic systems such as facet-engineered and aluminum-doped strontium titanate⁴. Furthermore, these regimes are associated with anisotropic facets and defect structures; hence, they can provide insights into the rational design of photocatalysts with significantly improved performance.

Methods

Sample preparation

All Cu₂O single photocatalyst particles were prepared by an electrodeposition method similar to that reported previously³². The deposition was performed in a standard three-electrode setup, in which glass substrates coated with a SnO₂:F layer (FTO), platinum foil, and saturated Ag/AgCl electrode were used as the working electrode, counter electrode, and reference, respectively. The facet ratio of the Cu₂O particles was tuned by tuning the ratios of NO₃⁻ and SO₄²⁻ ions in the precursor solution for electrodeposition because NO₃⁻ and SO₄²⁻ ions favor the stabilization of the {001} and {111} facets of Cu₂O, respectively³³. For the synthesis of Cu₂O particles with systematic shape evolution from cube to octahedron, the precursor solution used was a mixture of 0.02 M of Cu(NO₃)₂ and 0, 0.01, 0.02, 0.03, and 0.05 M of Na₂SO₄. The pH of the solution was adjusted to 4.9 prior to deposition. The Cu₂O particles with morphological evolution were deposited galvanostatically at a current density of 0.45 mA cm⁻² and a deposition time of 800 s from the precursor solution at 60 °C in a water bath. The scanning electron microscopy (SEM) images in Extended Data Fig. 1 show that all Cu₂O particles are well crystallized with similar particle sizes of 5–6 μm, and the morphology of the Cu₂O crystallites changes systematically from cube through truncated cube, truncated octahedra with comparable proportions of the {001} and {111} facets and with dominant {111} facets, to octahedral as the Na₂SO₄ concentration is increased from 0 to 0.05 M.

Defect engineering was performed on the truncated octahedral Cu₂O particles. The defects were tuned using the deposition current density²⁹. For the series of defect-engineered Cu₂O particles, the current

densities were maintained at 0.45 (E-Cu₂O), 0.6 (EH-Cu₂O), and 0.9 (H-Cu₂O), respectively, during deposition. The potentials achieved at the end of the depositions were 28, 3, and -23 mV, respectively, with respect to the Ag/AgCl reference (Extended Data Fig. 3a). During the electrochemical growth of the Cu₂O particles, the Cu²⁺ ions were reduced to Cu₂O through the following chemical reaction: $2\text{Cu}^{2+} + \text{H}_2\text{O} + 2\text{e}^- \rightarrow \text{Cu}_2\text{O} + 2\text{H}^+$. At a low deposition current and reduction potential (low dose of reductive e⁻), excess Cu²⁺ was generated, resulting in V_{Cu}. A higher deposition current and reduction potential resulted in the formation of a higher concentration of hydrogen that compensated for the V_{Cu} defects and the formation of (H-V_{Cu}) defects¹⁹. Therefore, tuning of the deposition current, in principle, enables defect engineering. To maintain the anisotropic truncated octahedral shape, the precursor solution was adjusted to a mixture of 0.02 M of Cu(NO₃)₂ and 0.03, 0.02, and 0.01 M of Na₂SO₄ for E-Cu₂O, EH-Cu₂O, and H-Cu₂O, respectively, and the integrated charge was 0.36 As/cm² for all samples such that all samples maintained a similar particle size (Extended Data Fig. 3b).

Au was deposited on the Cu₂O samples using the photodeposition method. The precursor solution for the photodeposition contained 20 μM of HAuCl₄, and a mixture of methanol and deionized water (volume ratio, 1:20). HAuCl₄ was used as the precursor, and methanol was used as a hole scavenger. Typically, Cu₂O particles grown on an FTO sheet would be immersed into a precursor solution and irradiated by a 300 W Xe lamp (λ > 420 nm) for 60 s.

Scanning probe microscopy

AFM, KPFM, SPVM, and C-AFM measurements were performed under an ambient atmosphere using a commercial AFM system (Bruker Dimension Icon). Pt/Ir-coated Si tips with a spring constant of 1–5 N m⁻¹ and resonance frequency of 60–100 kHz (Bruker SCM-PIT) were used for all measurements. For the KPFM measurements, the surface potential (CPD) images and signals of the samples were measured in the amplitude-modulated (AM-KPFM) mode at an AC voltage of 0.5 V. During the measurement of the surface potential, the lift mode was used with minimal lift height to minimize possible cross-talk artifacts from the compensation of the tip and cantilever³⁴. For the imaging of a single particle, the lift height was set to 30–50 nm for ensuring good image quality. For the quantitative signal measurements, the lift height was set to ~0 nm. In the lift mode, the topography and surface potential signals were recorded sequentially.

The SPV is the difference in the CPD before and after illumination, expressed as $\text{SPV} = \text{CPD}_{\text{light}} - \text{CPD}_{\text{dark}}$ ¹⁷. SPVM measurements were conducted by continuously mapping the surface potential images in the dark and under illumination via KPFM. The difference between the surface potential images obtained via illuminated and dark KPFM scans at the same location was extracted as an SPVM image¹⁰. For typical SPVM images, a 450 nm laser with a light intensity of approximately 5 mW/cm² was used to excite the sample. A modulated method was used to measure the SPV signals quantitatively. A chopper was placed between the light source and the sample at a frequency of 6 Hz. The tip was scanned over an

extremely small region (typically approximately 10 nm) to obtain the average of the surface potential signal while maintaining the spatial resolution. Furthermore, 6 Hz light-modulated CPD signals were exported from the front panel of the Nanoscope V controller using a BNC connector fed into an external SR830 DSP lock-in amplifier and synchronized with the chopped signal. The modulated SPV signals obtained after the operation of the external lock-in amplifier yielded an energy resolution of less than 5 mV, and the cross-talk artifacts were negligible. To measure the dependence of the SPV signals on the light wavelength, wavelength-tunable monochromatic light was obtained from a 300 W Xe arc lamp (PLS-SXE300, Beijing Perfectlight Co. Ltd)) using a Zolix Omni- λ 500 monochromator and focused on the sample via a series of lenses. To measure the dependence of the SPV signals on the light power, a 450-nm laser equipped with a neutral density filter was used, thereby enabling a tunable range of light power from 0 to 100 mW/cm².

I–V curve measurements via C-AFM were performed in the PeakForce TUNA mode. During the measurements, the tip was fixed onto the surface of the Cu₂O particles. The I–V curves were recorded by sweeping the sample bias from negative (-5 V) to positive (5 V) values. At a positive bias voltage, electrons were injected from the tip into the Cu₂O particle and then collected by the FTO back contact. To measure the photocurrent, a 450 nm laser with 5 mW/cm² light intensity was used.

TR-PEEM

This setup was located at the X-ray photoemission electron microscopy end station of the Dreamline (BL09U) at the Shanghai Synchrotron Radiation Facility. TR-PEEM measurements were enabled by combining the femtosecond pump–probe technique and PEEM system²². The oscillator (FLINT, Light Conversion) output 6 W pulses of less than 100 fs width at a center wavelength of 1030 nm and a repetition rate of 76 MHz. The second-order harmonic 515 nm (2.4 eV) laser pulse served as the pump pulse, whereas the fourth-order harmonic 257.5 nm (4.8 eV) served as the probe pulse. The cross-correlation of this scheme was approximately 184 fs. The measurements were performed under ultrahigh vacuum conditions of approximately 2×10^{-10} Torr, and the sample was heated at 200 °C for degassing before the measurements. The PEEM images were recorded at a series of pump–probe delays, and the time-resolved photoelectron yield was obtained by summing the signal of the selected area in each PEEM image. Time-resolved micro-area photoelectron spectra (PES) were obtained in an area measuring 1.5 μ m in diameter. The time-resolved and facet-dependent SPV signals were acquired from the shifts in the peak position of the PES at different pump–probe delays obtained on each facet.

Transient SPV spectroscopy

Transient SPV spectroscopy measurements were performed in a fixed-capacitor arrangement^{30,35}. The SPV signals were coupled with high-impedance buffers (measurement resistance, 50 G). The SPV transients were excited with pulses from a tunable Nd:YAG laser (EKSPLA NT342/1/UVE). The duration and repetition rates of the laser pulses were 4 ns and 1 Hz, respectively. The transients were detected with

a resolution time of 5 ns (GaGe CS 14200). A logarithmic read-out based on a logarithmic averaging procedure was applied to register the SPV transients³⁶.

Raman microscopy

Facet-dependent Raman spectroscopy and Raman imaging were performed using a Renishaw InVia confocal Raman microscope equipped with an Olympus 100x objective. A laser emitting at 532 nm was used for the excitation.

XPS

XPS analysis was performed on freshly prepared Cu₂O samples using a Thermo ESCALAB 250Xi spectrometer with a monochromatic Al K_α source (1486.6 eV) at 15 kV and 10.8 mA. The binding energies were calibrated in relation to the C1s peak at 284.6 eV.

SEM

The morphology of the samples was analyzed via SEM using a Quanta 200 FEG scanning electron microscope. The operating voltage was 30 kV.

UV-vis absorption spectroscopy

The absorbance was measured using a UV-vis spectrophotometer (JASCO V-650) by measuring the diffuse reflection spectrum.

DFT calculations

DFT calculations were performed using the Perdew–Burke–Ernzerhof functional with the VASP code. A planewave cutoff of 400 eV and a k-point sampling of 4 × 4 × 1 for stoichiometric Cu₂O were used. Defects were calculated in 2 × 2 periodic Cu₂O {001} and {111} slabs with ~15 Å vacuum between the slabs.

Simulations of charge transfer using drift-diffusion model

The simulations were performed based on Poisson and continuity equations that reflected the drift–diffusion model. The continuity equation was first used to describe the charge transfer in the interfacet built-in electric field; it is expressed as³⁷

$$\frac{\partial \Delta p(x,t)}{\partial t} = D_p \cdot \frac{\partial^2 \Delta p(x,t)}{\partial x^2} - \mu_p E \cdot \frac{\partial \Delta p(x,t)}{\partial x} - \mu_p \cdot \Delta p(x,t) \frac{\partial E}{\partial x} - \frac{\Delta p(x,t)}{\tau_p} \quad (1)$$

where $\Delta p(x,t)$ is the excess hole density, D_p is the hole diffusion coefficient, μ_p is the hole mobility, and E is the electric field. E , corresponding to the x -coordinate, is a finite difference. Therefore, E can be regarded

as a constant in each of the differential units. Hence, the continuity equation can be simplified to

$$\frac{\partial \Delta p(x,t)}{\partial t} = D_p \cdot \frac{\partial^2 \Delta p(x,t)}{\partial x^2} - \mu_p E \cdot \frac{\partial \Delta p(x,t)}{\partial x} - \frac{\Delta p(x,t)}{\tau_p} \quad (2)$$

The electrons follow the similar description

$$\frac{\partial \Delta n(x,t)}{\partial t} = D_n \cdot \frac{\partial^2 \Delta n(x,t)}{\partial x^2} - \mu_n E \cdot \frac{\partial \Delta n(x,t)}{\partial x} - \frac{\Delta n(x,t)}{\tau_n} \quad (3)$$

where $\Delta n(x,t)$ is the excess electron density, D_n is the electron diffusion coefficient, and μ_n is the electron mobility. The separation and transfer of photogenerated electrons and holes in the built-in electric field induced a reversed electric field, known as the photoinduced electric field (E_p)¹², and impeded further charge transfer. E_p can be calculated using the Poisson equation, as follows

$$\frac{\partial E_p(x,t)}{\partial x} = - \frac{e(\Delta n(x,t) - \Delta p(x,t))}{\epsilon_0 \epsilon_r} \quad (4)$$

By solving the continuity equations shown in Equations (2) and (3), substituting the excess electron and hole density into the Poisson equation shown in Equation (4), and integrating E_p over the propagation distance (d), we obtain the SPV as follows

$$SPV(t) = \int_0^d E_p(x,t) dx = \sum_{i=1}^n \frac{d}{n} E_p(i \frac{d}{n}) \quad (5)$$

Therefore, we used the evolution of the SPV with time to describe the charge transfer in the built-in electric fields (Extended Data Fig. 7d). To calculate $SPV(t)$, the following parameters were used: propagation distance $d = 680$ nm, doping density $N = 10^{14}$ cm⁻³ (d and N were determined from potential distribution fits in Extended Data Fig. 7b), dielectric constant $\epsilon_0 = 8.85 \times 10^{-12}$ F/m, $\epsilon_r = 7.2$,³⁸ and $\mu_p = 50$ cm² V⁻¹ s⁻¹.³⁹ The hole diffusion coefficient D_p was calculated from the hole mobility based on the Einstein relationship. Two cases were considered when calculating $SPV(t)$. In one case, the carriers were cooled at room temperature (298 K), and D_p was calculated to be 1.25 cm²/s. In the other case, the carriers were in a non-equilibrium state (without any carrier scattering) at a temperature of ~ 5000 K, calculated as follows⁴⁰

$$T = \frac{(E_{ph} - E_g)}{k_0} \quad (6)$$

where $E_{\text{ph}} = 2.4$ eV is the energy of the incident photons, $E_{\text{g}} \sim 2.0$ eV is the optical bandgap of Cu_2O , and k_0 is the Boltzmann constant.

Photocatalytic measurements

Photocatalytic reactions were performed in a Pyrex top-irradiation-type reaction vessel connected to a closed gas circulation system. Typically, Cu_2O particles grown on 2×2 cm FTO sheets are immersed in 0.5 M Na_2SO_3 solution (150 mL). The mass of the Cu_2O particles was calculated to be approximately 1 mg based on the integrated charge during the electrochemical synthesis of Cu_2O particles. Na_2SO_3 is the optimized hole scavenger for photocatalytic hydrogen generation by Cu_2O , according to a previous study⁴¹. The system was evacuated to ensure complete air removal and then irradiated from the top side using a 300 W Xe lamp (Ushio-CERMAX LX300). Cooling water was flowed to maintain the reaction suspension at 288 K. The evolved H_2 gases were analyzed via on-line gas chromatography (Shimadzu GC-8A, TCD, Ar carrier).

Declarations

Acknowledgements

This work was supported by the National Natural Science Foundation of China (Grant Nos. 22088102, 21633015 and 21773228), Chinese Academy of Sciences Interdisciplinary Innovation Team (Grant No. JCTD-2018-10), Dalian Institute of Chemical Physics Innovation Foundation (Grant No. DICPSZ201801).

Author Contributions

R.C. and F.F. conceived the research. R.C. carried out most of the experiments, analysed and interpreted all the experimental data, and wrote the manuscript. Z.R., Y.L. and G.Z. collected and analysed TR-PEEM data. T.D. performed transient SPV spectroscopy measurements. S.P. performed DFT calculations and assisted in simulations. Y.Z. assisted in photocatalytic activity measurements. H.A. assisted in Raman microscopy measurements. F.F. and C.L. supervised the project. Z.R., T.D., F.F. and C.L. discussed the data and revised the manuscript.

Competing interests

The authors declare no competing financial interests.

References

1. Wang, Q. *et al.* Scalable water splitting on particulate photocatalyst sheets with a solar-to-hydrogen energy conversion efficiency exceeding 1%. *Mater.* **15**, 611-615 (2016).
2. Lewis, N. S. Developing a scalable artificial photosynthesis technology through nanomaterials by design. *Nanotechnol.* **11**, 1010-1019 (2016).

3. Hisatomi, T. & Domen, K. Reaction systems for solar hydrogen production via water splitting with particulate semiconductor photocatalysts. *Nat. Catal.* **2**, 387-399 (2019).
4. Takata, T. *et al.* Photocatalytic water splitting with a quantum efficiency of almost unity. *Nature* **581**, 411-414 (2020).
5. Wang, D. *et al.* Identifying the key obstacle in photocatalytic oxygen evolution on rutile TiO₂. *Nat. Catal.* **1**, 291-299 (2018).
6. Baxter, J. B., Richter, C. & Schmittenmaer, C. A. Ultrafast carrier dynamics in nanostructures for solar fuels. *Annu. Rev. Phys. Chem.* **65**, 423-447 (2014).
7. Esposito, D. V. *et al.* Methods of photoelectrode characterization with high spatial and temporal resolution. *Energy Environ. Sci.* **8**, 2863-2885 (2015).
8. Delor, M., Weaver, H. L., Yu, Q. & Ginsberg, N. S. Imaging material functionality through three-dimensional nanoscale tracking of energy flow. *Nat. Mater.* **19**, 56-62 (2020).
9. Sambur, J. B. *et al.* Sub-particle reaction and photocurrent mapping to optimize catalyst-modified photoanodes. *Nature* **530**, 77-80 (2016).
10. Chen, R. *et al.* Charge separation via asymmetric illumination in photocatalytic Cu₂O particles. *Nat. Energy* **3**, 655-663 (2018).
11. Chen, R., Fan, F., Dittrich, T. & Li, C. Imaging photogenerated charge carriers on surfaces and interfaces of photocatalysts with surface photovoltage microscopy. *Chem. Soc. Rev.* **47**, 8238-8262 (2018).
12. Yang, Y. *et al.* Semiconductor interfacial carrier dynamics via photoinduced electric fields. *Science* **350**, 1061-1065 (2015).
13. Selim, S. *et al.* Impact of Oxygen Vacancy Occupancy on Charge Carrier Dynamics in BiVO₄ Photoanodes. *J. Am. Chem. Soc.* **141**, 18791-18798 (2019).
14. Wu, Y. A. *et al.* Facet-dependent active sites of a single Cu₂O particle photocatalyst for CO₂ reduction to methanol. *Nat. Energy* **4**, 957-968 (2019).
15. Li, R. *et al.* Spatial separation of photogenerated electrons and holes among {010} and {110} crystal facets of BiVO₄. *Nat. Commun.* **4**, 1432 (2013).
16. Selcuk, S. & Selloni, A. Facet-dependent trapping and dynamics of excess electrons at anatase TiO₂ surfaces and aqueous interfaces. *Nat. Mater.* **15**, 1107-1112 (2016).
17. Kronik, L. & Shapira, Y. Surface photovoltage phenomena: theory, experiment, and applications. *Surf. Sci. Rep.* **37**, 1-206 (1999).
18. Scanlon, D. O., Morgan, B. J., Watson, G. W. & Walsh, A. Acceptor levels in p-type Cu₂O: rationalizing theory and experiment. *Phys. Rev. Lett.* **103**, 096405 (2009).
19. Scanlon, D. O. & Watson, G. W. Uncovering the complex behavior of hydrogen in Cu₂O. *Phys. Rev. Lett.* **106**, 186403 (2011).

20. Sander, T. *et al.* Correlation of intrinsic point defects and the Raman modes of cuprous oxide. *Phys. Rev. B* **90**, 045203 (2014).
21. Warren, S. C. *et al.* Identifying champion nanostructures for solar water-splitting. *Nat. Mater.* **12**, 842-849 (2013).
22. Man, M. K. *et al.* Imaging the motion of electrons across semiconductor heterojunctions. *Nat. Nanotechnol.* **12**, 36-40 (2017).
23. Doherty, T. A. S. *et al.* Performance-limiting nanoscale trap clusters at grain junctions in halide perovskites. *Nature* **580**, 360-366 (2020).
24. Najafi, E., Scarborough, T. D., Tang, J. & Zewail, A. Four-dimensional imaging of carrier interface dynamics in p-n junctions. *Science* **347**, 164-167 (2015).
25. Sung, J. *et al.* Long-range ballistic propagation of carriers in methylammonium lead iodide perovskite thin films. *Nat. Phys.* **16**, 171-176 (2019).
26. Borgwardt, M. *et al.* Femtosecond time-resolved two-photon photoemission studies of ultrafast carrier relaxation in Cu₂O photoelectrodes. *Nat. Commun.* **10**, 2106 (2019).
27. Long, J. P., Sadeghi, H. R., Rife, J. C. & Kabler, M. N. Surface space-charge dynamics and surface recombination on silicon (111) surfaces measured with combined laser and synchrotron radiation. *Phys. Rev. Lett.* **64**, 1158-1161 (1990).
28. Najafi, E., Ivanov, V., Zewail, A. & Bernardi, M. Super-diffusion of excited carriers in semiconductors. *Nat. Commun.* **8**, 15177 (2017).
29. Chen, R. *et al.* Giant Defect-Induced Effects on Nanoscale Charge Separation in Semiconductor Photocatalysts. *Nano Lett.* **19**, 426-432 (2019).
30. Dittrich, T., Fengler, S. & Franke, M. Transient surface photovoltage measurement over 12 orders of magnitude in time. *Rev. Sci. Instrum.* **88**, 053904 (2017).
31. Zhu, J. *et al.* Visualizing the Nano Cocatalyst Aligned Electric Fields on Single Photocatalyst Particles. *Nano Lett.* **17**, 6735-6741 (2017).
32. Siegfried, M. J. & Choi, K. S. Electrochemical crystallization of cuprous oxide with systematic shape evolution. *Adv. Mater.* **16**, 1743-1746 (2004).
33. Siegfried, M. J. & Choi, K. S. Elucidating the effect of additives on the growth and stability of Cu₂O surfaces via shape transformation of pre-grown crystals. *J. Am. Chem. Soc.* **128**, 10356-10357 (2006).
34. Barbet, S. *et al.* Cross-talk artefacts in Kelvin probe force microscopy imaging: A comprehensive study. *J. Appl. Phys.* **115**, 144313 (2014).
35. Dittrich, T. *et al.* Temperature dependent transient surface photovoltage spectroscopy of a Cu_{1.95}Zn_{1.1}Sn_{0.96}Se₄ kesterite single phase powder. *Appl. Phys. Lett.* **110**, 023901 (2017).
36. Dittrich, T., Bonisch, S., Zabel, P. & Dube, S. High precision differential measurement of surface photovoltage transients on ultrathin CdS layers. *Rev. Sci. Instrum.* **79**, 113903 (2008).

37. de Jongh, P. E. & Vanmaekelbergh, D. Trap-limited electronic transport in assemblies of nanometer-size TiO_2 particles. *Phys. Rev. Lett.* **77**, 3427-3430 (1996).
38. Yang, Y. C. et al. Facet-dependent optical properties of polyhedral Au- Cu_2O core-shell nanocrystals. *Nanoscale* **6**, 4316-4324 (2014).
39. Lee, S., Liang, C. W. & Martin, L. W. Synthesis, Control, and Characterization of Surface Properties of Cu_2O Nanostructures. *ACS Nano* **5**, 3736-3743 (2011).
40. Liao, B. et al. Photo-excited hot carrier dynamics in hydrogenated amorphous silicon imaged by 4D electron microscopy. *Nat. Nanotechnol.* **12**, 871-876 (2017).
41. Toe, C. Y. et al. Photocorrosion of Cuprous Oxide in Hydrogen Production: Rationalising Self-Oxidation or Self-Reduction. *Angew. Chem. Int. Ed.* **57**, 13613-13617 (2018).
42. Poulston, S., Parlett, P. M., Stone, P. & Bowker, M. Surface oxidation and reduction of CuO and Cu_2O studied using XPS and XAES. *Surf. Interface Anal.* **24**, 811-820 (1996).
43. Petroff, Y., Yu, P. Y. & Shen, Y. R. Study of photoluminescence in Cu_2O . *Phys. Rev. B* **12**, 2488-2495 (1975).
44. de Jongh, P. E., Vanmaekelbergh, D. & Kelly, J. J. Photoelectrochemistry of electrodeposited Cu_2O . *J. Electrochem. Soc.* **147**, 486-489 (2000).
45. Scanlon, D. O. & Watson, G. W. Undoped n-Type Cu_2O : Fact or Fiction? *J. Phys. Chem. Lett.* **1**, 2582-2585 (2010).
46. Malerba, C. et al. Absorption coefficient of bulk and thin film Cu_2O . *Sol. Energy Mater. Sol. Cells* **95**, 2848-2854 (2011).

Figures

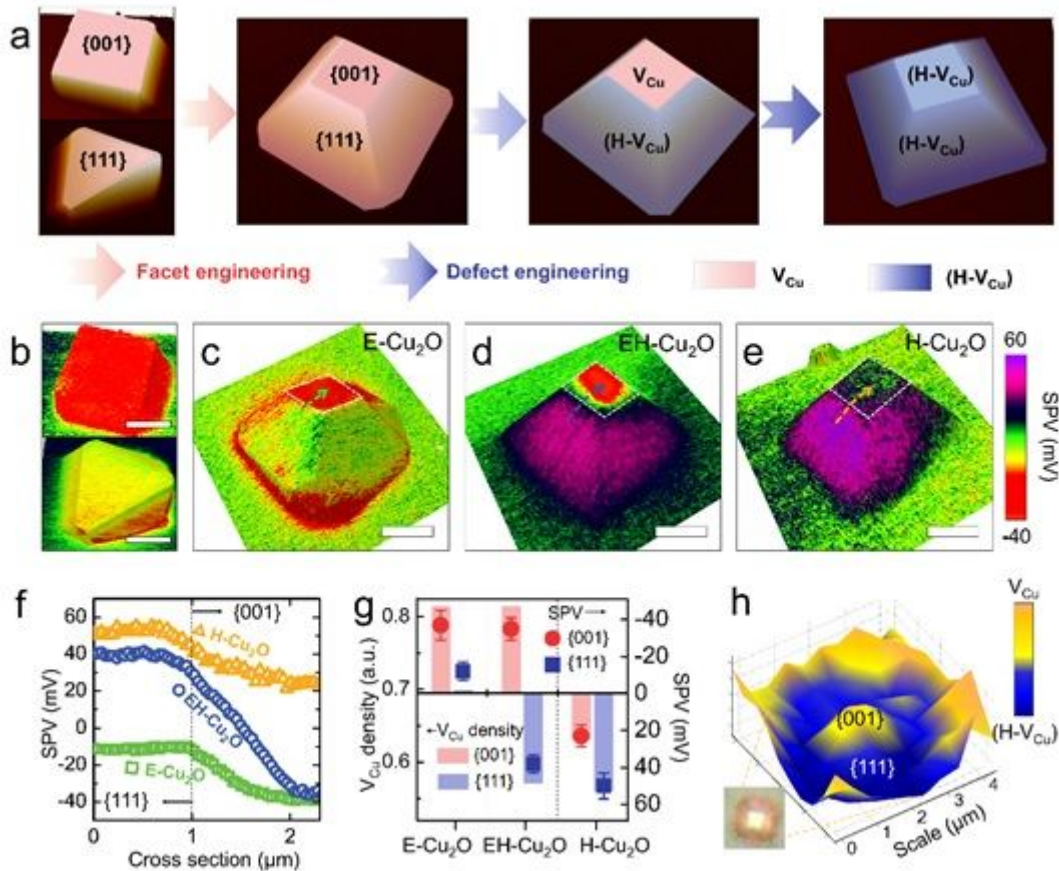


Figure 1

Anisotropic structure engineering and surface charge distribution mapping. a, Illustration of anisotropic engineering of facets and defects of Cu_2O photocatalyst particles. b, SPVM images of cubic and octahedral Cu_2O particles. c–e, SPVM images of truncated octahedral Cu_2O particles without (c), with moderate (d) and with extreme (e) incorporation of $(H-V_{Cu})$ defects. All scale bars are 2 μm . SPVM images are mapped with 450 nm and 5 mW/cm² light illumination. f, SPV values extracted across dashed lines in c–e. g, Quantitative correlation between V_{Cu} density and SPV values. V_{Cu} density recorded with normalized V_{Cu} -related Raman intensity (Extended Data Fig. 4f). SPV values are statistically averaged by pixels extracted from corresponding SPVM images with electronic noise as error bars. h, Confocal Raman microscopy image of EH- Cu_2O particle mapped with V_{Cu} -related Raman peak intensity. Low Raman intensity denotes $(H-V_{Cu})$, which compensates for V_{Cu} .

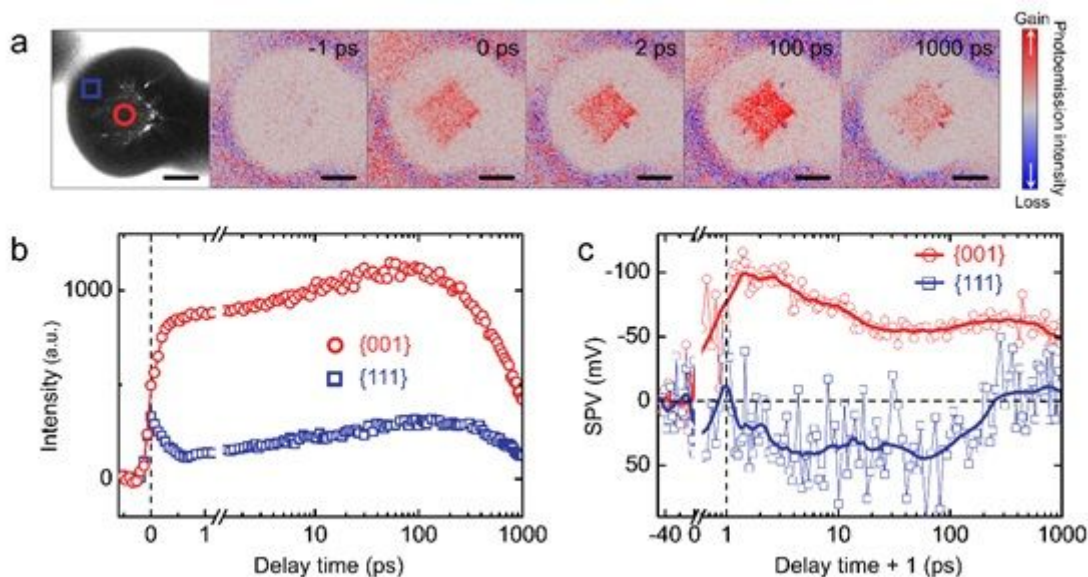


Figure 2

Time-resolved photoemission electron microscopy of EH-Cu₂O particles. a, PEEM image and sequence of TR-PEEM images of an EH-Cu₂O particle captured at different pump-probe delays, as labeled. A reference image, captured at -2 ps, is subtracted to eliminate background signals. A 515 nm laser pulse was used to excite sample (pump) and frequency doubled to 257 nm as a time-delayed probe. Scale bars, 2 μ m. b, Photoemission electron intensity plotted as a function of pump-probe delay time collected on the {001} and {111} facets of an EH-Cu₂O particle, as indicated in the PEEM image in a. c, Transient SPV signals plotted as a function of pump-probe delay time collected on the {001} and {111} facets of EH-Cu₂O particles by extracting peak shifts from time-resolved photoelectron spectroscopy (Extended Data Figs. 6f,g). The delay time in x axis was shifted by 1 ps to show SPV evolution in the logarithmic time scale. The solid lines are smooth lines from experimental data points.

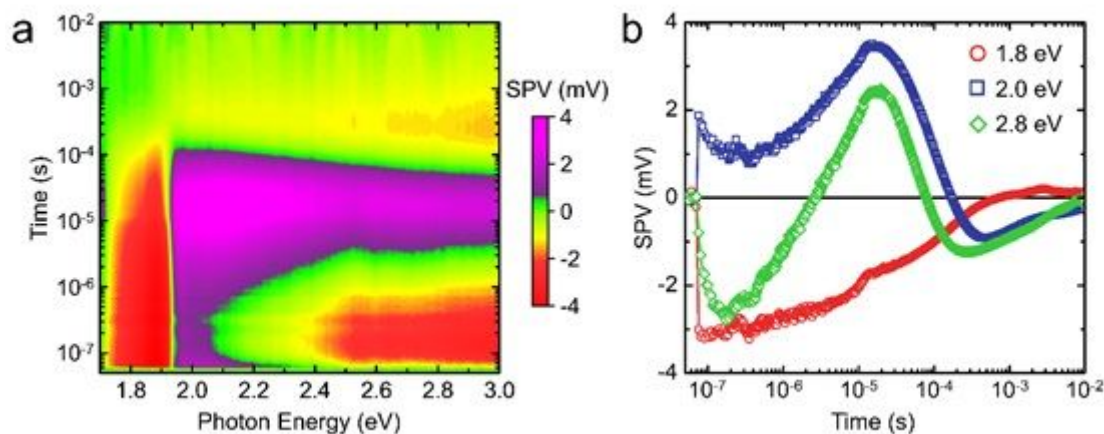


Figure 3

Transient SPV spectroscopy of EH-Cu₂O. a, Pseudocolor image of spectral and time-dependent distributions of SPV signals for EH-Cu₂O. Color intensity indicated by color scale bar represents SPV

signals. b, SPV transients of EH-Cu₂O extracted from a at photon energies of 1.8, 2.0, and 2.8 eV.

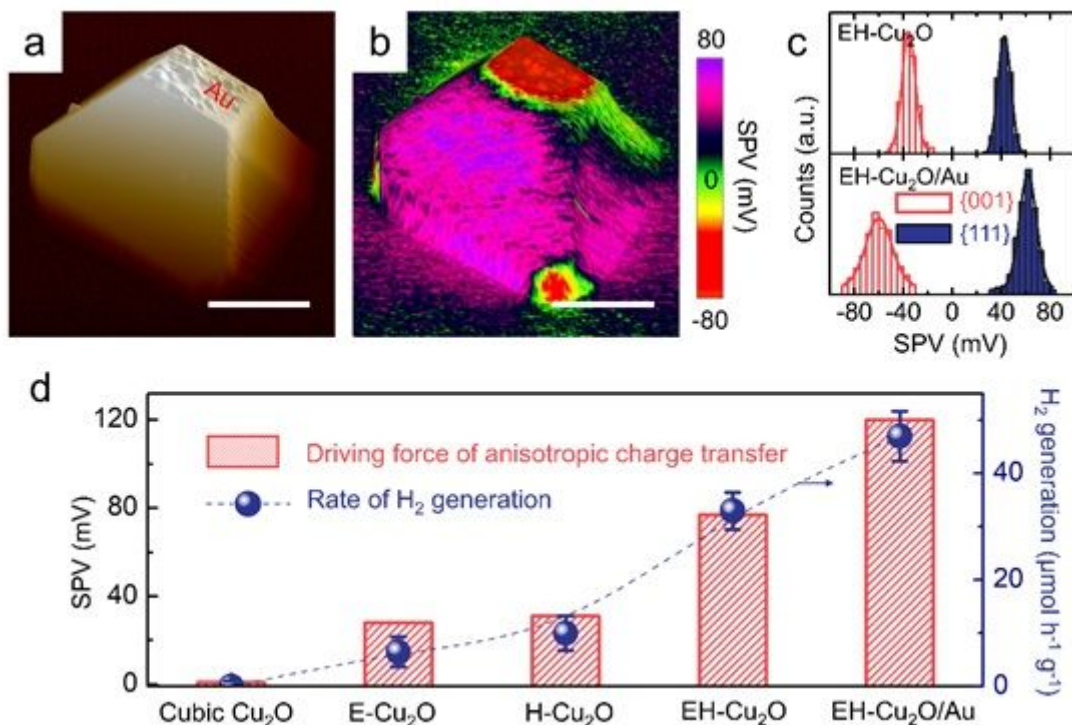


Figure 4

Selective co-catalyst loading and photocatalytic performance. a,b, AFM image (a) and corresponding SPVM image (b) of EH-Cu₂O particle with selective deposition of Au particles on the {001} facet (denoted as EH-Cu₂O/Au). Scale bars, 2 μm. c, Comparison of statistical SPV signals of {001} and {111} facets between EH-Cu₂O and EH-Cu₂O/Au particles. d, Driving force of anisotropic charge transfer and rate of photocatalytic hydrogen generation in different Cu₂O photocatalytic systems. Driving forces are extracted via vector sum of spatially resolved SPV signals. Error bars show standard deviations. Photocatalytic reactions performed using 0.5 M of Na₂SO₃ as a hole scavenger under 300 W Xe lamp illumination.

Supplementary Files

This is a list of supplementary files associated with this preprint. Click to download.

- [SupplementaryMovie.avi](#)
- [ExtendedDataFigures.pdf](#)